Postprint of: Błaszczak P., Ducka A., Wolanin B., Matlak K., Machowski G., Prześniak-Welenc M., Wang S., Bochentyn B., Jasiński P., Fabrication of wormhole-like YSZ and Ni-YSZ by the novel soft-hard template CTAB/NaCl-assisted route. Suppressing Ni coalescence in SOFC, JOURNAL OF THE EUROPEAN CERAMIC SOCIETY Vol. 43, iss. 2 (2023), pp. 438-451, DOI: 10.1016/j.jeurceramsoc.2022.09.054

Fabrication of wormhole-like YSZ and Ni-YSZ by the novel soft-hard template CTAB/NaCl-assisted route. Suppressing Ni coalescence in SOFC

Patryk Błaszczak[(a)*], Agata Ducka[(a)], Barbara Wolanin[(b)], Krzysztof Matlak[(b)], Grzegorz Machowski[(c)], Marta Prześniak-Welenc[(a)], Sea-Fue Wang[(d)], Beata Bochentyn[(a)], Piotr Jasiński[(e)]

[(a)] Advanced Materials Center, Faculty of Applied Physics and Mathematics, Gdansk University of Technology, 80-233 Gdańsk, ul. Narutowicza 11/12, Poland
[(b)] National Synchrotron Radiation Centre SOLARIS, Jagiellonian University, Czerwone Maki 98, 30-392 Kraków, Poland
[(c)] Faculty of Geology, Geophysics and Environmental Protection, AGH University of Science and Technology, al. A. Mickiewicza, 30-059 Kraków, Poland
[(d)] Department of Materials and Mineral Resources Engineering, National Taipei University of Technology, 1, Sec. 3, Zhongxiao E. Rd., Taipei, 106 Taiwan
[(e)] Advanced Materials Center, Faculty of Electronics, Telecommunications and Informatics, Gdansk University of Technology, 80-233 Gdańsk, ul. Narutowicza 11/12, Poland

*corresponding author: patryk.blaszczak@pg.edu.pl

Abstract

A novel one-pot synthesis route leading to the formation of a wormhole-like structure was developed for the successful fabrication of porous YSZ and Ni-YSZ systems. This method involved co-precipitation in the presence of the micelle-forming agents CTAB/Pluronic P123 and crystallising NaCl. The obtained skeletons were mechanically stable and presented almost 50% uniform, open porosity without using any additional pore-formers. The fabricated 0.3 M CTAB/NaCl Ni-YSZ showed better long-term electrical stability in hydrogen than a traditional Ni-YSZ cermet. It resulted from the suppression of Ni structural changes throughout the anode scaffold. Moreover, higher electrochemical activity of this novel anode is expected due to the smaller particle sizes of Ni/YSZ, high homogeneity, highly developed TPB, and better interfacial interaction between the Ni and YSZ. Therefore, the novel soft-hard templating method is recognised as a promising route for the fabrication of the YSZ or Ni-YSZ with a highly developed microstructure and improved stability.

Keywords: YSZ, cermet, SOFC, agglomeration, conductivity

1. Introduction

Solid Oxide Fuel Cells (SOFCs) are electrochemical devices that are emerging as a future source of electrical energy. Their high working temperatures offer high electrochemical efficiency, leading to their high specific power and making them attractive for many applications [1]. The high temperature working conditions make it possible to utilise fuels other than pure hydrogen, e.g., methane, biogas, or ethanol [2]. Such a device in its most primitive form comprises three major components: a porous anode and cathode separated by a gas-impermeable electrolyte that can only conduct ionic species between the electrodes [3]. The principal role of the anode is the oxidation of the gaseous fuels and the generation of electrons flowing through the external load, generating power. It is also responsible for the efficient mass transfer of the reactants and products within its bulk to prevent significant concentration polarisation [4]. The most widely used material for the fabrication of the SOFCs' anodes is the NiO-YSZ composite, which forms Ni-YSZ cermet on reduction. This is due to its high electrical and ionic conductivity and good electrochemical activity in relation to its relatively low price [5]. Aside from this, it provides sufficient mechanical strength, and its thermal expansion coefficient matches that of the electrolyte, what prevents delamination.

The electrochemical activity at the anode site in SOFCs increases with the increase in the reaction area created by the triple phase boundary (TPB) [6]. The performance of the anode is greatly influenced not

only by the properties of the constituents but also by microstructural parameters such as grain size, amount of components, spatial distribution or contiguity of the subphases [5,7]. Over the years, there was done loads of research concerning the microstructural alterations of the NiO-YSZ to enhance its performance in SOFCs. Those are mostly based on the studies concerning various methods of powders preparation [8], NiO-YSZ ratios [9], powder milling schemes [10], and 3D shaping of the conventional slurries [11]. Byeongseok K. *et al.* [12] prepared a NiO-YSZ composite by a 2-step hydrothermal route and applied the material as an anode functional layer. The composite fabricated this way showed much higher conductivity than the one prepared using ball milling and allowed a single cell to reach a power output of 1.7 W cm^{-2} at 800 °C. In parallel, Song J. H. *et al.* [13] synthesised nanopowders of NiO-YSZ (~100 nm diameter) using a co-precipitation method with subsequent hydrothermal treatment. The generated power of the cell equipped with the novel cermet material was higher than when the cell was fabricated using conventional methods. The studies of Cho H. J. *et al.* [4] revealed that even the milling steps of the NiO and YSZ starting powders have a crucial influence on the final performance of the SOFC. Implementation of high energy milling ensured much lower particle sizes than when the normal ball milling was used. It was found that the polarization resistance was greatly minimized, and the single cell power output was increased from ~500 mW cm^{-2} up to 850 mW cm^{-2} at 800 °C.

Another branch of the studies into the improvement of the NiO-YSZ composite entails structural modification via novel methods in the shaping of the conventional slurries. Numerous research papers have already been published in the field of 3D shaping of the electrolyte and electrodes to effectively increase the working surfaces of the components [11,14,15]. Current research of Jang I. *et al.* [16] on 3D inkjet-printed Ni(O)-YSZ pillar structures revealed that restructuring the anode-electrolyte interface can increase the SOFC and SOEC power performance by a factor of 1.5, and 3, respectively. In contrast, Betke U. *et al.* [17] fabricated cellular Ni(O)-YSZ composites via a sponge replication technique. The materials were fully characterised, and the authors stated that geometric factors can variously influence the electrical and mechanical properties.

The chemical processes, in general, often yield powders that enable better performance of the electrodes, but are considered more laborious and complicated, and thus expensive [18–20]. Therefore, the mass production of SOCs mostly follows mechanical processing schemes, and all slurries are being made via ball milling. To increase the market value of the bottom-up chemical processes, the complexity and utilisation of exotic feedstock should be limited.

Herein, a novel, one-pot synthesis route for the 8YSZ ($Zr_{0.84}Y_{0.16}O_2$) and NiO-YSZ composites is presented. Implementing a dual soft-hard templating method based on a micelle-forming system composed of CTAB/Pluronic P123 and crystallising NaCl produced a wormhole-like microstructure of the materials. Although no external pore former was used, high porosities of around 50% could be maintained after a high-temperature sintering step due to the synergistic effect of the organics and high-temperature removal of NaCl. The fabricated materials were subjected to a series of characterisations comparing them to the state-of-the-art conventional materials found in mass-scale cells. Co-precipitation of the NiO-YSZ composite in the assistance of CTAB/NaCl thoroughly dispersed the NiO grains that were highly integrated with the YSZ support. Further long-term degradation tests revealed that the novel material structure exhibited a reduced degradation rate and better microstructural stability under SOFC working conditions.

2. Experimental

2.1. Synthesis of the wormhole-like structures

All the materials were prepared using our novel and simple preparation technique based on precipitation from aqueous solutions enriched with a micellar system for templating. Depending on the final product to be obtained, the proper amount of precursor salts $ZrCl_4$ (Alfa Aesar, 98%), YCl_3*6H_2O (Alfa Aesar,

99.9%), $NiCl_2*6H_2O$ (Chempur, 98%) was weighed and placed into a beaker. The composition of the Ni-YSZ cermet was set to 60:40 by volume. Later, a micelle-forming system composed of CTAB (cetyltrimethylammonium bromide, Alfa Aesar, 98%) and Pluronic P123 (PEG-PPG-PEG, Merck, M_n~5800) was added to the inorganic salts. The chosen concentration of CTAB was set to 25CMC, corresponding to 25 times the amount of the critical micelle concentration in DI water at RT (~25 mM). Pluronic P123 was added as a micelle-stabilising agent at a concentration of 1 mM. The amounts were established based on previous studies on the influence of the concentration of the micelle-forming system on the final properties of the sintered YSZ. Everything was topped up with the appropriate amount of DI water to create 0.1, 0.2, 0.25, 0.3, 0.4, and 0.5 M final solutions of the metal cations.

The solution was heated up to 70 °C and stirred until a clear solution was obtained. The precursor solution was cooled down to RT using an ice bath. The calculated amount of the precipitation agent in the form of NaOH (POCH, 99.9%) was added to a small beaker, dissolved in 20 cm^3 of DI water and brought down to RT. The precipitate solution was then added in 5 cm^3 increments to the heavily stirred YSZ or NiO-YSZ precursor solutions until a pH of ~10 was reached and a gel formed. The content of the beaker was stirred for 1 h and aged for 12 h to fully react the chlorides. The gel was then separated using centrifuge. Next, the wet gel was collected after decanting the supernatant, and dried at 80 °C overnight. The xerogels were ground using planetary mill equipped with ZrO_2 milling jars and are referred to further in the text as 'precursor powders'. After a final drying step at 80 °C, the precursor powders were ready for further characterisation and processing.

2.2. Preparation of the pellets and description of the reference materials

The pellets for the conductivity measurement were prepared by uniaxial dry pressing of the precursor powders at a pressure of 45 MPa. Next, the green pellets were placed onto alumina plates and sintered at 1400 °C (YSZ) and 1370 °C (NiO-YSZ) for 4 h.

The reference YSZ scaffold from conventional cell build-up was prepared according to our previous experience with the cell modifications. Conventional NiO-YSZ-based half-cells fabricated by tape casting were provided by the National Taipei University of Technology. The cells consisted of a 400 μm 60:40 by vol. NiO-YSZ anode with bimodal porosity (anode functional layer – AFL and supporting gas-transfer layer) and a thin ~8–10 μm YSZ electrolyte. The half-cells were reduced at 800 °C and etched with the mixture of 30 vol.% HNO_3 with a few drops of HCl at 80 °C. The etching was performed while periodically changing the acid solution until there was no evidence of Ni dissolution. The etched scaffolds were then rinsed with a bunch of DI water and strengthened by sintering at 1300 °C for 2 h. This step increased the intergranular cohesion between the YSZ grains without significantly altering the pore structure.

2.3. Characterisation methods

Diffraction patterns of the as-prepared and sintered precursor powders were collected using a Bruker D2 PHASER XE-T with a Cu-Kα radiation source. The free-flowing powder morphology and cross-sections of the pellets after sintering, prereduction, and electrical measurements were verified using a scanning electron microscope (SEM, FEI Quanta FEG 250) with an energy dispersive x-ray spectroscope (EDX, EDAX Genesis APEX 2i) and Apollo X SDD detector.

The values of the total and open porosity of the pellets were calculated by the means of the Archimedes principle of density measurement. The dry samples were first weighed then immersed in kerosene and subjected to vacuum treatment at RT until no more bubbling occurred. The soaked samples were reweighed when submersed in the kerosene and in ambient air after the removal of excess surficial fluid. The calculations were performed according to the standard procedure of the Archimedes density and

porosity measurements [21]. The relative linear shrinkage (Δd) was additionally calculated using the following equation (1):

$$\Delta d = \frac{d_g - d_s}{d_g} \cdot 100\ \% \quad (1)$$

where d_g and d_s are the diameters of the green and sintered pellets, respectively.

The specific surface area (SSA) was measured based on the BET isotherm model on an N_2 sorption unit (NOVAtouch LX1, Quantachrome). Prior to the sorption measurements, the samples were subjected to adsorbate removal under a high vacuum at 300 ℃ for 3 h.

Studies of the pore space via the MICP (Mercury Injection Capillary Pressure) method were performed using a mercury porosimeter (AutoPore IV 9520, Micromeritics). The samples were dried prior to analysis at 105 °C for at least 24 h to remove any moisture from the pore spaces. The analysis was carried out assuming sample evacuation to 50 μm Hg (6.67 Pa) for 2 min and an equilibrium time of 10 s. The pressure was measured at 120 points in the range of 1.7–60,000 psi (0.01–413.7 MPa). To calculate the average pore diameter and the total pore area, the Washburn equation based on the behaviour of a non-wetting liquid was used. The contact angle was assumed to be 130 °.

The reduction behaviour of the Ni-YSZ with the novel microstructure was investigated through cyclic temperature-programmed techniques involving reduction (H_2-TPR) and oxidation (O_2-TPO) measurements. The tests were done using our custom-designed TPx system with a base containing a TCD detector provided by Buck Scientific, USA. The pellets made of novel the NiO-YSZ and a reference, conventional cell were ground to the form of powders. 100 mg of the material was placed inside the reactor tube and degassed prior to the measurements under flowing He at 200 °C for 20 mins. The H_2-TPR cycles were performed in a stream of 40 ml min^{-1} 5 vol.% H_2 in Ar up to 800 °C with a heating rate of 10 °C min^{-1}. The O_2-TPO tests were carried out under a flow of 5 vol.% O_2 in He. The flow rate and heating regime were the same as for the reduction tests. The reduction/oxidation profiles data was collected with a frequency of 1 Hz using the PeakSimple software. The cyclic tests were used to determine the changes in the degradation rates between the new Ni-YSZ structure and the conventional one.

The thermal expansion coefficient was examined using a Netzsch DIL 402 PC dilatometer working in the 100–1000 °C temperature range under a synthetic air stream at a 3 °C min^{-1} heating-cooling rate.

Simultaneous thermogravimetry (TG) and differential scanning calorimetry (DSC) measurements were performed under synthetic air on a Netzsch STA 449 F1 Jupiter apparatus coupled with a 403 C Aëolos quadrupole mass spectrometer. The data was collected from room temperature to 1370 °C at a heating rate of 5 °C min^{-1}.

Novel Scanning Transmission X-ray Microscopy (STXM) measurements were performed on the 0.3 M CTAB/NaCl NiO-YSZ precursor powder at the SOLARIS National Synchrotron Radiation Centre (Kraków, Poland). The used synchrotron energy range ensured the collection of the images before and on the Ni-$L_{2,3}$ and Na-K edges of the as-prepared Ni-YSZ precursor powder to reveal the distribution of the cations and subphases across the powder before sintering. The STXM imaging was performed on the powders finely dispersed onto a Si_3N_4 membrane. The series of image stacks were collected under a He atmosphere. Detection of the transmitted radiation was performed using a photomultiplier tube (PMT). The collected images were analysed using the aXis 2000 software. The elemental maps were formed as the difference between the scan collected at the absorption edge and the one performed much before the absorption region.

2.4. Experimental methods of electrical testing

The electrical conductivity of the anode-like porous pellets was measured by the Van der Pauw (VdP) method using our custom-built unit. The pellets were first polished on both sides to remove the possible Ni-depleted area that may form due to the direct contact between the pellet and the alumina substrate during high-temperature sintering. Four Pt reversible electrodes were brushpainted onto the corners of the square-shaped pellets and dried at 150 °C for 30 mins. The electrical contacts in the form of Pt wires were attached to the previously prepared electrodes using Ag conductive paste and air dried until a solid connection was obtained. The measuring unit was placed in a high-temperature furnace and a steady stream of the selected gas was set. The measurement was performed according to the standard scheme of the VdP method using a Keithley 2400 SourceMeter. An automatic logging system and our own software were used for data collection. The YSZ scaffolds were heated in a stream of synthetic air (SynAir, AirLiquide) up to 800 °C and measured every 25 °C down to 400 °C with a stabilisation time of 30 mins for each step. For the NiO-YSZ samples, the pellets were heated in a stream of N_2 (Air Liquide, 4N5) protective gas and reduced by switching to 3 vol.% H_2O humidified H_2 at 800 °C. After conditioning at 800 °C for 1 h, the samples were subjected to the same testing regime as described above. The raw datasets were used to calculate the apparent electrical conductivity (σ) according to the equation (2):

$$\sigma = \frac{ln2}{\pi h} \frac{2}{R_{AB,CD} + R_{CA,DB}} \quad (2)$$

where: σ is the apparent conductivity of the sample, h is the thickness of the pellet, $R_{X,Y}$ is the measured resistance, which is determined by switching the current applied to two electrodes and measuring the potential between the other pair of the electrodes. No additional approximations to the conductivity of the porous samples was enabled to present the as-seen results of the conductivity in the inhomogeneous samples. The long-term tests were performed in humidified H_2 with constant collection of the resistances every 1 min.

3. Results

2.1. Composition and structure of the starting materials

The phase composition of the prepared precursor powders and sintered pellets was determined by the XRD diffraction technique, and the results are presented in Fig. 1. One can find that the precursor powders were of low crystallinity and composed of multiple phases (Fig. 1, left). The peaks that overwhelm the XRD pattern came from the halite (NaCl) *Fm-3m* cubic phase that formed during the powder drying step. It illustrates that a high amount of salt was left behind within the structure after the synthesis steps. The rest of the unidentified peaks were recognised as the ones that came from the mixed oxyhydroxides/hydroxides of Zr, Y, and Ni. Only subtle and very broad peaks related to the ZrO_2-like phase could be definitively recognised. Even though the peaks coming from NaCl were observed, the salt did not form the highly crystalline and well-defined 3D structure of cube-like crystals. The XRD results of the 0.3 M CTAB/NaCl YSZ and NiO-YSZ sintered pellets will be covered and discussed in the further part of the manuscript.

An exemplary SEM image of the 0.3 M CTAB/NaCl YSZ precursor powder is presented in the Supplementary Materials (Fig. S1). The structure of the xerogel after the milling step is spongy and flaky with no clearly observable crystal structures formed. The low intensity milling step was able to ensure a good homogeneity of the precursor powders. Larger clusters were also observed as the powder tended to agglomerate due to the highly developed surface area and tendency to take up moisture from the air, even though the amorphous particles of the precipitated oxyhydroxides were well distributed and encapsulated within the NaCl matrix.

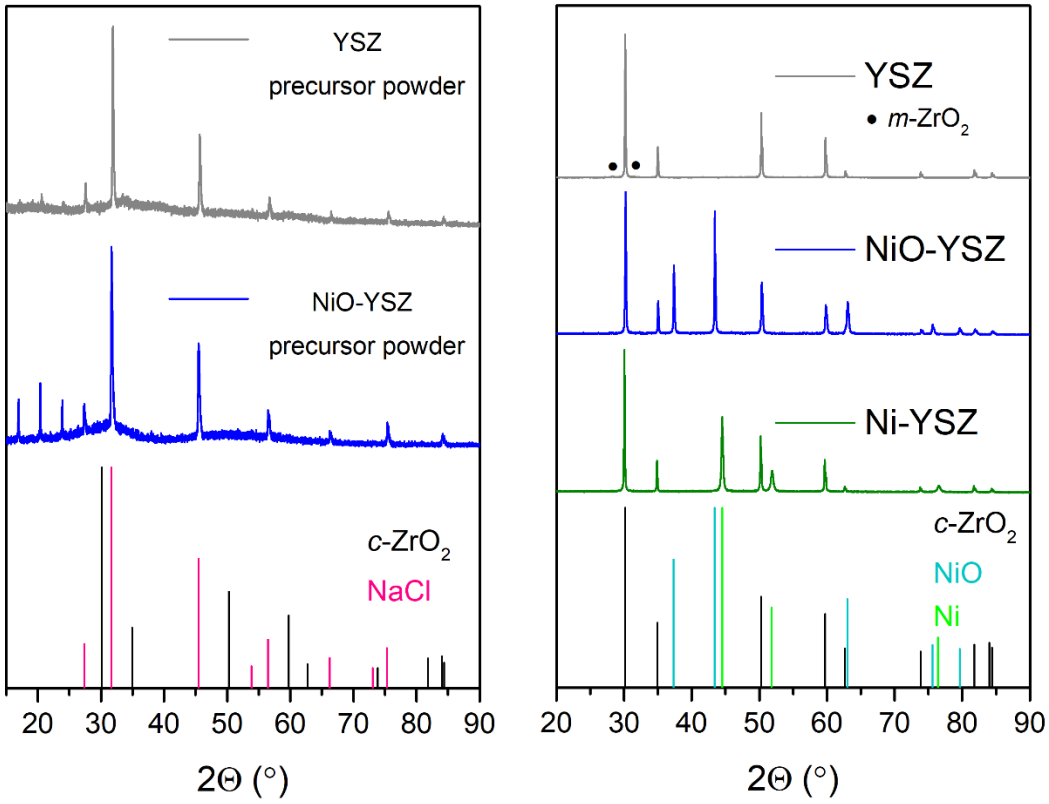

Fig. 1. XRD diffraction patterns of the precursor powders (left) and sintered pellets (right) showing full removal of the NaCl upon sintering.

A similar structure was observed by SEM in the case of the 0.3 M CTAB/NaCl NiO-YSZ precursor powder (Fig. 2, right) prepared in the same way as the 0.3 M CTAB/NaCl YSZ but replacing part of the Y-Zr cations with Ni to form 60:40 by volume NiO-YSZ composite. Despite the morphological similarities, the 0.3 M CTAB/NaCl NiO-YSZ precursor powder revealed a higher tendency towards agglomeration and created a matrix of intermixed Ni and Zr-Y oxyhydroxides with no clear distinction between the Ni and Y-Zr phases. There are visible nanoparticles of oxyhydroxides embedded within big agglomerates of low-crystallinity NaCl. The distribution of the Ni subphase was also studied using synchrotron radiation-based STXM imaging. A series of the images was collected at 848 eV (before the Ni edge), 853 eV (Ni edge) and 1070 eV (Na edge, Fig. S2). The two Ni images were used to prepare an Ni elemental map. The results are shown in Fig. 2. The absorption edge energy is very close to that of the NiO phase but located in the lower energy region with pre-peak necking that may indicate a slightly increased average valence over +II. This is due to the existence of NiO(OH), which formed in parallel to NiO during the low temperature synthesis process [22]. In the transmission images taken at the Ni absorption edge, one can see that the Ni is rather homogeneously distributed within the imaging area. Where the particle size is at the threshold of the permittivity for a beam to pass the sample, the absorption of Ni compounds fully blackened the main image areas. On the other side, the areas with smaller precursor powder grains (Fig. 2, indicated in red frames) were selectively darkened for the clusters with a higher Ni content. Those gave clear evidence the Ni formed highly submicrometric precipitates embedded within the rest of the gel. As this was unlikely to be homogeneous YSZ precipitation, it was not certain if the phases containing Ni and Zr/Y cations will form in parallel or whether they would create a homogenous mixture in the case of one-pot CTAB/NaCl NiO-YSZ co-precipitation. In fact, a clear separation of both precipitates occurred. It was caused by the huge difference in the thermodynamics parameters of the $Ni(OH)_2$ precipitation from $NiCl_2$ compared to the $Zr(OH)_4$-$Y(OH)_3$ system. Based on the calculations performed using the HSC Chemistry software

(Outotec), the exothermic neutralisation reaction of $NiCl_2$ with NaOH was characterised by a 2–3 times lower absolute value of ΔH_{303K} (-47.4 kcal mol^{-1}) than the rest of the metal salts (Zr: -163.1 kcal mol^{-1}; Y: -103.4 kcal mol^{-1}). Followed by the higher ΔS_{303K}, $Ni(OH)_2$ tended to instantaneously form at 30 °C, much ahead of the Zr-Y hydroxides, due to the thermodynamic limitations caused, e.g., by the increasing temperature of the reaction volume [23,24]. It resulted in the good separation of both composite subphases despite the formation of the nanoprecipitate. Additionally, the low tendency of the Ni to get dissolved into YSZ cubic lattice ensures no interdiffusion of NiO and YSZ while sintering. In this way, it is possible to obtain a homogeneous structure of high entanglement with good separation of the components during one-pot synthesis. The STXM image collected at the Na absorption edge (Fig. S2) indicated that all the precipitated metal (oxy)hydroxides-oxides were dispersed uniformly within the NaCl matrix which, later on, acted as a high-temperature pore former and a flux, leaving behind the wormhole-like structure of the NiO-YSZ anode. Unfortunately, Zr and Y edges could not be detected due to the radiation energy limits of the synchrotron facility.

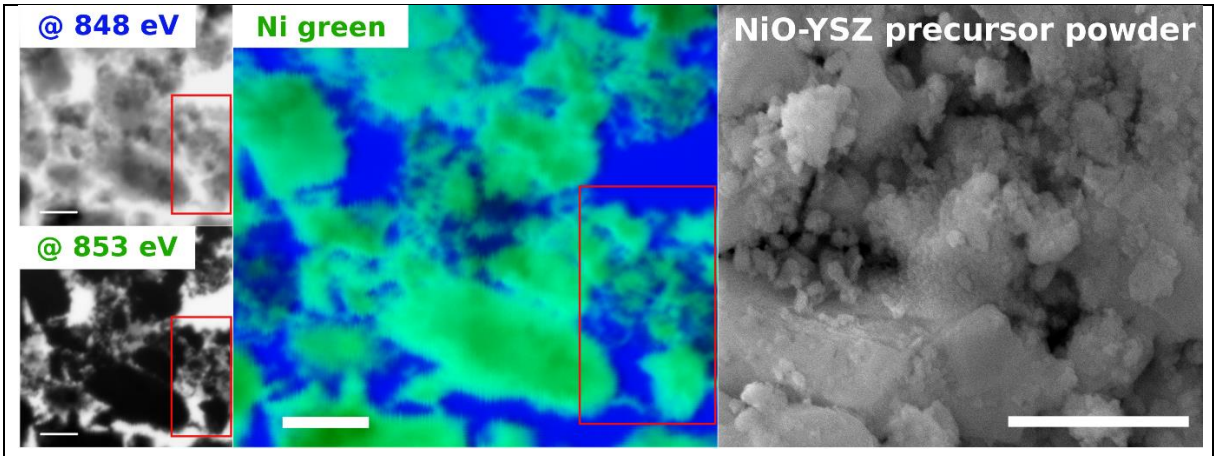

Fig. 2. STXM images of the 0.3 M CTAB/NaCl NiO-YSZ precursor powder measured at 848 eV (before the Ni edge), 853 eV (Ni edge), Ni elemental map and SEM image. Every scale bar is 1 µm. Red frames indicate the area of higher permittivity for the radiation.

After the sintering step of the precursor powders at 1400 °C and 1370 °C, respectively, highly crystalline products of YSZ and NiO-YSZ were obtained. In the case of the 0.3 M CTAB/NaCl NiO-YSZ, the sintering temperature of 1400 °C produced a fully dense pellet. The decrease of the temperature to 1370 °C was necessary to maintain the wormhole-like structure of the 0.3 M CTAB/NaCl NiO-YSZ. Exemplary XRD diffractograms of the 0.3 M CTAB/NaCl YSZ and NiO-YSZ sintered pellets are shown in Fig. 1. Sintering at 1400 °C produced a nearly pure cubic *Fm-3m* YSZ phase with traces of a monoclinic *P21/c* ZrO_2 phase. The content of the cubic stabilised phase of ZrO_2 and monoclinic ZrO_2 were calculated by Rietveld refinement to be equal to 99.2% and 0.8%, respectively. The unit cell parameter (a=b=c) of the 0.3 M CTAB/NaCl YSZ was 5.129 Å, which is close to the previously presented values for 8 mol.% YSZ, and indicates the formation of the assumed ion-conducting phase [25,26]. A small amount of the monoclinic phase may arise from local depletion of the Y dopant concentration or a slightly too-low sintering temperature of the YSZ pellets. In fact, the amount of secondary phase in the bulk material is so low that its influence on the global ionic conductivity can be neglected. The formation of the cubic phase of the desired stoichiometry directly proved the synthesis method to deliver well-dispersed powders of intermixed Y and Zr hydroxides with no obvious intermixing of the Ni precipitate with the Y and Zr ions. The XRD pattern of the sintered 0.3 M CTAB/NaCl NiO-YSZ (Fig. 1, right) revealed, at first sight, that two separate phases of the cubic NiO (*Fm-3m*) and 8YSZ had formed during the sintering step. Even so, the unit cell parameters calculated by Rietveld refinement were slightly lower (5.125 Å) than for the pure 8YSZ. According to the work of

Linderoth S. *et al.* [27], lower values of the 8YSZ lattice parameters were observed after incorporating the minimal amounts of Ni^{2+} into the YSZ structure. Further on, the Ni-doped YSZ was subjected to reduction in H_2 and the particles of Ni were exsolved from the single-phase material [28]. A similar situation was most probably also encountered in this study, where a small amount of ultra-fine precipitate of NiO dissolved into the YSZ lattice during the sintering step at high temperature. The solubility limit of the NiO in the undoped ZrO_2 lattice is extremely low (~2 mol.%) and hard to obtain by simply reacting the bulk substrates [29]. When yttrium is introduced to stabilise the ZrO_2 cubic phase, the NiO solubility limit increases, but it is considered that it is not higher than 5 mol.% [30]. In the CTAB/NaCl method, the NiO dissolved into YSZ due to the nanometric effects, but the amount of the NiO in the NiO-8YSZ solid solution was also considered very low. To estimate the amount of NiO dissolved in the YSZ lattice forming a solid solution, the equation (Eq. 3) given by Kuzjukevics A. *et al.* [30] was used, where $a_{NiO-YSZ}$ is the lattice parameter of YSZ with NiO dissolved, and $m_{YO_{1.5}}$ and m_{NiO} are the molar contents (%) of $YO_{1.5}$ and NiO dissolved into the lattice, respectively.

$$a_{NiO-YSZ} = 0.5119 + 0.0001394 m_{YO_{1.5}} - 0.000515 m_{NiO} \quad (3)$$

It was estimated that the 8YSZ lattice contained ~1 mol.% of dissolved NiO after the sintering step, which is in line with the previous studies on NiO-YSZ interactions in nanocomposites [27,30]. Even so, the partial dissolution of the Ni ions into the YSZ was critical and resulted in the formation of Ni nanoparticles in the presented novel structures. This issue will be covered more thoroughly later in the text. In the case of the 0.3 M CTAB/NaCl Ni-YSZ (NiO-YSZ after reduction at 800 °C for 10 h in H_2), the XRD pattern revealed two phases, namely, cubic Ni (*Fm-3m*) and cubic 8YSZ. It should be noted that the diffraction peaks coming from the Ni phase were broadened. Considering the greyish-green colour of the sintered NiO-YSZ pellets, it was established that the CTAB/NaCl fabrication method leads to the formation of submicrometric grains of NiO. The presented novel synthesis method can limit the growth of the NiO grains despite its known tendency to sinter and coalesce. Smaller particles of Ni would result in a higher active surface area and an elongated triple-phase boundary (TPB) leading to decreased polarisation losses. The lattice parameters of the NiO and Ni were 4.168 Å, and 3.524 Å, respectively. Those values were identified as quite normal and widely described in the literature [31,32], so no clear evidence of contamination of the NiO grains with secondary elements (Zr, Y, Na) was found. SEM images of the YSZ pellets prepared via a novel synthesis route are presented in Fig. 3. The images were collected using the fractures of the porous samples sintered at 1400 °C. With the increasing concentration of the cation in the starting precursor solution, a clear change in the microstructure and porosity took place. The samples with the lowest (0.1 M) and highest (0.5 M) amount of metal cations were much denser than the other compositions. For the 0.1 M solution, the densification occurred due to the highly dispersed and strongly nanometric particles that formed during the precipitation step. In addition, the highly diluted precursor facilitated the formation of a loose and separated precipitate that did not retain the organic phase within the structure of the gel. The increase in the concentration of cations was followed by the increasing development of the specific surface area (SSA) reached its final look for the concentration of 0.3 M–0.4 M, where the most interesting interstructures formed. A further increase in the starting cation concentration resulted in higher densification rates, and the porosity was lost. During the preparation step, it was established that the starting precipitate was forming big chunks that were highlight likely to agglomerate. When compared to the enormous amount of the formed hydroxide precipitate, the fixed share of organic additives lost its template properties and the porous structure could not be maintained while sintering.

In the case of intermittent concentrations of cations, a clear change in the microstructure was visible as a network of small particles of rounded shape had formed. The diameter of the particles varied around 400 nm. Highly porous scaffold composed of sintered particles with interconnected channels and the

structure was referred to further in the text as a ‘wormhole-like YSZ structure’. SEM images of the structure of the etched YSZ reference material are included in the Supplementary Materials as Fig. S3 for comparison.

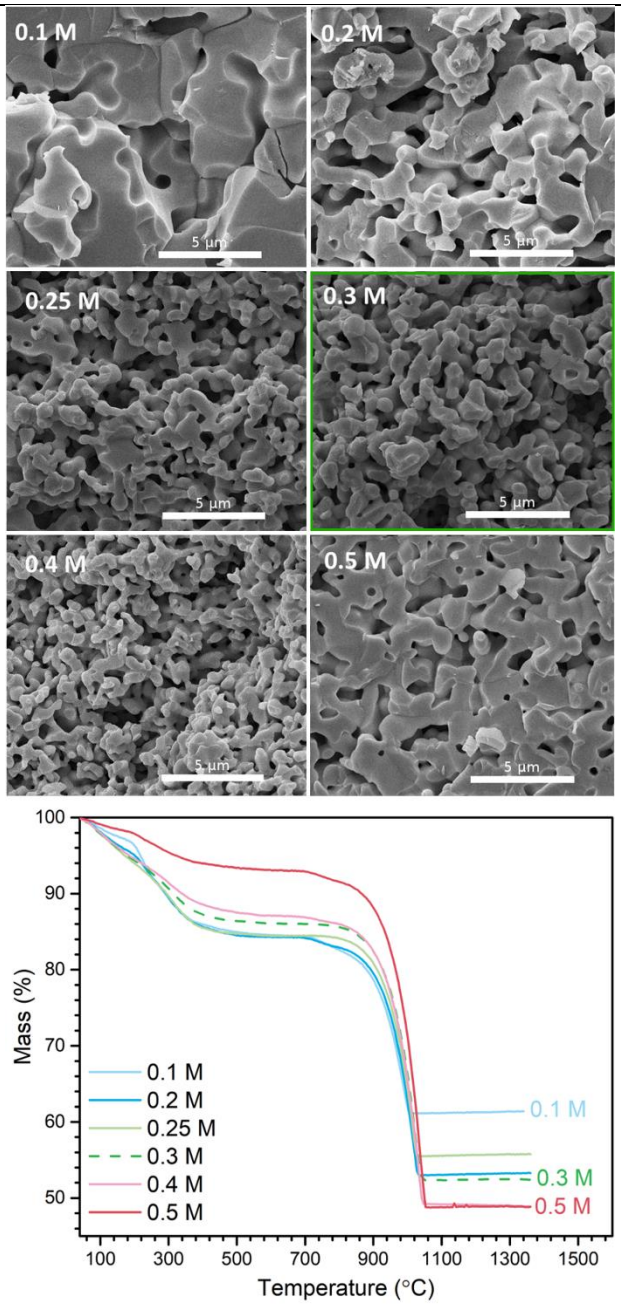

Fig. 3. SEM images of the sintered YSZ scaffolds (top) and TGA curves of the YSZ precursor powders (bottom) prepared using the CTAB/NaCl templating method. Green frame indicates the sample of the highest porosity.

Even though no external pore former was used (e.g., PMMA, graphite, starch), the structure remained porous even after high-temperature treatment. If one considers such a structure as one of the SOFC anode components, it can be stated that the obtained microstructure provides a high active surface area for the distribution of the oxygen ions throughout a Ni-YSZ composite. The additional benefit is the usage of a small amount of the organics (CTAB/P123), which, despite their minor concentration, makes it possible to achieve high porosity and a homogeneous structure of the scaffold. The reasons behind the formation of the shown microstructure are twofold. First, the decomposition and burnout of the organic

template separates the YSZ grains, as with conventional pore formers. In parallel, the NaCl coming from the precursor salts crystallised within the structure during the neutralisation reaction and powder drying steps. Up to the melting point of the salt, the structure remains supported by the present NaCl hard template, which limits the densification of the pellets. In fact, the previous studies involved the clean-up of the obtained gel with DI water prior to the sintering step. The removal of the salt resulted in obtaining dense pellets of the YSZ, proving the crucial role of NaCl in the formation of wormhole-like pores. This is both beneficial for the manufacturing process, as no pore formers can be used, and for the environment, as only minor gaseous species are being released during the burnout.

To better describe the processes during the sintering, TG/DSC measurements of the precursor powders were performed. The results of the thermogravimetry analysis for the YSZ precursor powders with different metal cation concentrations are presented in Fig. 3 (right). A clear mass loss occurs at temperatures varying from 50 °C to 1000 °C, resulting in a final mass of about 45–60% of the initial mass. The thermogravimetric curve can be divided into two clearly distinguishable regions: up to 400 °C, and 800–1050 °C. The presence of the first mass drop results directly from the removal of absorbed water, followed by a burnout of CTAB/P123 organics [33]. The latter region of the TG curve is characterised by a drastic weight loss corresponding to the melting of NaCl, and with a further increase in the temperature, also intense salt volatilisation. The melting-volatilisation process is finished at 1050 °C, which is much lower compared to the vaporisation point of NaCl, but the obtained results are in line with the TGA of pure NaCl performed by Wang X. *et al.* [34]. The most significant decrease was observed for the 0.5 M YSZ, which can be explained by the high concentration of chloride ions in the 0.5 M solution and high amount of densely packed precipitate that formed. In contrast, the lowest concentration of CTAB/P123 in the 0.5 M dried precursor led to the smallest weight loss in the low-temperature regime. An analogous explanation can be given for the 0.1 M precursor powder, which is characterised by the smallest weight decrease at higher temperatures, originating from the lowest amount of the salt formed in the dried xerogel.

To provide even deeper insight into the sintering process, thermogravimetric/differential scanning calorimetry measurements were performed on the 0.3 M CTAB/NaCl YSZ and 0.3 M CTAB/NaCl NiO-YSZ precursor powders. TG/DSC curves are given in Fig. 4A. The first mass loss is attributed to the loss of the residual structural water remaining in the precursor powders. At 273 °C and 293 °C for NiO-YSZ and YSZ, respectively, burnout of the CTAB and other organics occurs [33], resulting in the formation of an endothermic peak on the DSC curve and conspicuous mass loss. The decomposition of CTAB was also confirmed by mass spectroscopy of the 0.3 M CTAB/NaCl YSZ, giving a maximum signal of CO_2 (m/z=44) at 294 °C. The QMID ion currents for a specific m/z are plotted in Fig. S4. The melting of NaCl in both precursors occurs at 800 °C, followed by evaporation at 1075 °C and 1047 °C for YSZ and cermet, respectively. The temperatures of the endothermic transitions are extremely close to those presented previously by Rocha C. *et al.* [35]. The melting and volatilisation of the salt are completed at 1080 °C with a final mass decrease of 50% (YSZ) and 51% (NiO-YSZ). The sintering of the precursors occurs above 1100 °C, as indicated by the formation of the endothermic valley and the decrease in the DSC heat flow. An additional endothermic peak seen for NiO-YSZ at approximately 1180 °C originates from the melting of the traces of Na_2O [36]. The presence of such a peak in only the cermet DSC curve results from the surplus amount of Na^+ ions added to the solution during the synthesis of NiO-YSZ. Interestingly, no traces of Na-rich phases were found in the XRD diffraction patterns, indicating that the excess of Na^+ does not affect the sintering process nor the final composition of the cermet. The endothermic valley ascribed to the sintering of the samples is much more visible for the NiO-containing sample as it is generally recognised that the addition of NiO into YSZ lowers the activation energy of the densification [37].

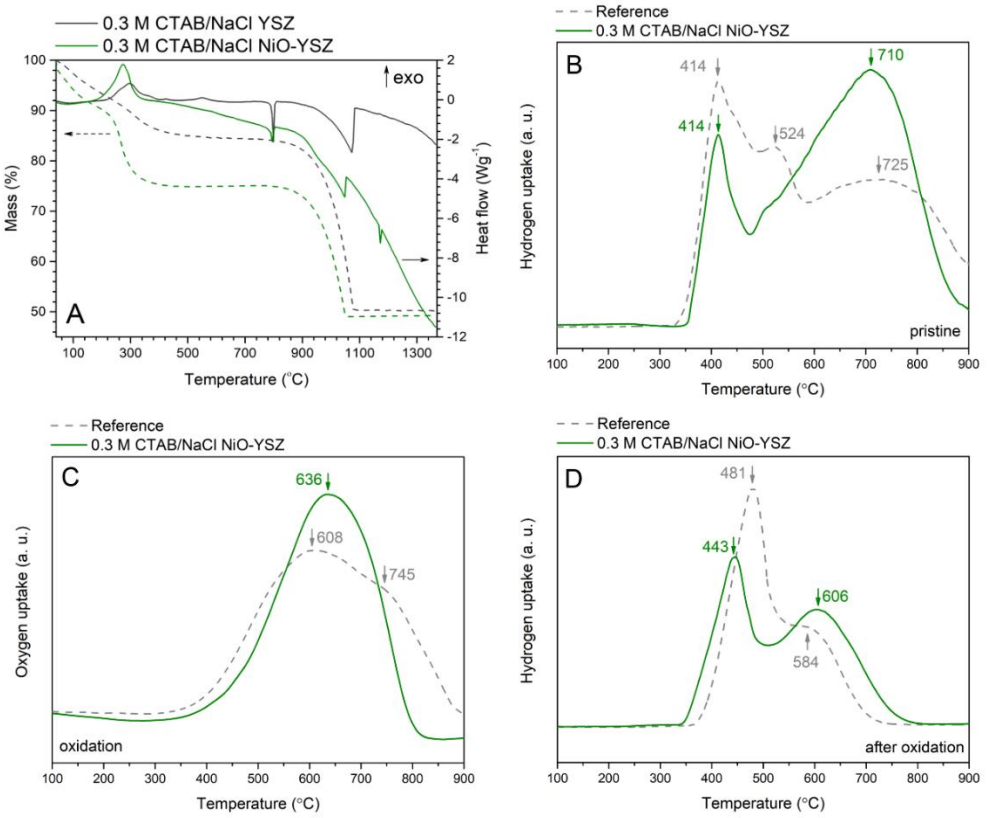

Fig. 4. A) TG-DSC curves of YSZ and NiO-YSZ precursors prepared via the CTAB/NaCl templating method, and B,C,D) differences in reducibility (TPR) and oxidation behaviour (TPO) of the novel 0.3 M CTAB/NaCl NiO-YSZ and the reference anode.

To better describe the metallic phase, a series of TPR and TPO studies were performed. The full cycle consisted of two reduction tests with an intermittent oxidation run. The results are shown in Fig. 4 B,C,D. The 0.3 M CTAB/NaCl NiO-YSZ sample was compared to the reference anode-supported cell from NTUT. The first reduction profile (Fig. 4B) of both the reference and 0.3 M CTAB/NaCl NiO-YSZ shown a peak at 414 °C, ascribed to the reduction of loosely bonded NiO particles [38]. With the reference sample, the peak at 524 °C corresponded to the reduction of an anode-functional layer of lower porosity with much bigger NiO grains. This behaviour was not observed for the 0.3 M CTAB/NaCl NiO-YSZ as no bimodal porosity was introduced. Moving on to the higher temperature region, the reduction peaks at around 700 °C for both materials were assigned to the reduction of strongly integrated NiO particles being in strong interfacial contact with YSZ grains. The slightly lower temperature of the 0.3 M CTAB/NaCl NiO-YSZ reduction was also characterised by significantly higher consumption of H_2 than in the case of the reference cell. Also, the reduction was completed within the testing temperature range and time, what did not take place with the reference sample. From the first reduction run (Fig. 4B), it is clearly visible that the CTAB/NaCl-assisted synthesis route ensured higher incorporation of the NiO into the YSZ substrate. At the same time, the reduction of those species is less limited by the mass transfer than for the reference material as the formed cermet particles are much smaller compared to the standard preparation route using the high-energy milling process [39]. The extent of the NiO-YSZ interaction strictly depends on the amount of NiO in the cermet. Under a low NiO content, the particles of NiO are usually well dispersed, and the aggregation starts to occur when the amount of NiO increases. The formation of the smaller NiO particles in the vicinity of the phase boundary is caused by the limited aggregation inhibited by the strong interaction between the NiO and YSZ [39–41]. The initial precursor structure (see Fig. 2, right) resulted in a more developed interface boundary between the NiO and Y_2O_3-

ZrO_2, which led to enhanced interdiffusion and anchorage of the NiO phase during the sintering step. The bimodal porosity of the reference sample was also visible during the oxidation test (Fig. 4C), where two maxima at 608 and 745 °C were detected. The first one was devoted to the oxidation of the gas-transfer base layer, whereas the oxidation peak at the higher temperature is most probably related to the bulk oxidation of the Ni grains in the anode-functional layer, where the grains are more tightly packed and bigger than in the supporting main layer. The 0.3 M CTAB/NaCl Ni-YSZ underwent complete oxidation peaking, monomodally at 636 °C. The novel cermet material was less prone to oxidation than the reference material despite the higher porosity. The mass transport of oxygen is more limited as the NiO is strongly embedded within the wormhole-like YSZ structure. The higher integration of NiO and YSZ resulted in the lower tendency towards NiO coalescence during reoxidation. To justify this statement, a secondary reduction was performed, and the results are presented in Fig. 4D. It was clearly evidenced that the growth of Ni-NiO grains in the 0.3 M CTAB/NaCl NiO-YSZ was limited. The primal 414 °C reduction peak shifted upwards much less (ΔT=29 °C vs. 67 °C for 0.3 M CTAB/NaCl NiO-YSZ and the reference cell, respectively), indicating smaller NiO particles in the wormhole-like structure than for the reference sample. At the same time, one can observe that the first reduction cycle fully decomposed both cermet materials as the high-temperature reduction peak was no longer detected. It agrees with the previous findings which suggested the splitting of the metastable NiO-YSZ solid solution and NiO embedded into the YSZ structure under a reducing atmosphere. The process is unavoidable and irreversible within the oxidation temperature up to 900 °C. The dissolution of NiO becomes kinetically accessible above 1200 °C [30,42,43]. Even so, in this case, clear evidence of the retained NiO-YSZ interfacial integration is visible (Fig. 4D) as the 0.3 M CTAB/NaCl NiO-YSZ still undergoes a high-temperature reduction process of relatively high intensity compared to the first one ascribed to the reduction of loose NiO particles. To sum up, the lower upward shift of the first reduction peak combined with the higher temperature of the secondary peak presenting a high relative intensity represents the lower tendency of NiO to migrate and coalesce, followed by the retention of the Ni-YSZ-anchoring interaction.

2.2. Microstructural and electrical characterisation of the modified anodes

The porosity of the YSZ pellets sintered at 1400 °C was examined by means of the Archimedes principle and the results are presented in Fig. 5, showing the distinction between the apparent (open) and total porosity. In each test, at least three samples of a specific composition were subjected to testing to provide reliable results and to decrease errors. The theoretical density of yttria-stabilised zirconia was taken as 6.1 g cm^{-3}. The porosity reaches its peak for a concentration of 0.3 M metal cations, being in line with the microstructures observed in the SEM images. For moderate concentrations of cations (0.2–0.4 M), the apparent porosity constitutes a significant contribution to the total porosity, while for extreme concentrations (0.1 and 0.5 M), the closed pores provide a considerable contribution to the overall porosity. For these concentrations, the porosity of the pellets cannot be maintained due to the high dispersion of the particles (0.1 M YSZ) or the formation of bigger agglomerates (0.5 M YSZ) during the preparation of the starting solutions. The closure of the pores and insufficient stabilisation of the CTAB/NaCl soft-hard templates have resulted in the annihilation of the wormhole-like structure. The reference material of Ni-etched YSZ was characterised by (66.1±1.2) % total porosity, while (64±1) % was open.

The porosity of the novel NiO-YSZ composite sintered at 1370 °C was measured, and its total porosity was found to be (36.1±0.4) %, of which (34±1) % was apparent. After reduction at 800 °C, the total porosity increased to (50±1) %, while the open porosity was found to be (48±1) %, which is comparably close to the values obtained for 0.3 M YSZ. Furthermore, Osinkin D. *et al.* [44] have proven that the

porosity of Ni-YSZ within the range of 40–50% can efficiently connect both the mechanical strength and good gas permeation through the anode. However, to increase the porosity of NiO-YSZ to the desired level, 5–15 wt.% of graphite had to be added as a pore former prior to the sintering, while the novel CTAB/NaCl-assisted route leads to the desired porosity without the use of any external additives. Beyond measuring the porosity of the samples, the relative shrinkage of the pellets after sintering was analysed and the results are presented in Fig. 5 (left) as blue dots (dashed lines are a visual guide only). To minimise the measurement error, several pellets of the same composition were surveyed. The relative linear shrinkage for all materials varied in a range of 30–40%, reaching its peak for the 0.3 M CTAB/NaCl YSZ (39.8±1.1) %. Interestingly, the relative linear shrinkage increases with the increasing porosity of the samples, indicating the biggest loss of additives present in the green pellets during the sintering, followed by the further growth of the YSZ grains. What is more, the samples synthesised by the CTAB/NaCl templating method are characterised by higher shrinkage values compared to yttria-stabilised zirconia manufactured by other methods and sintered at a similar temperature [45–48]. The relative linear shrinkage of the novel 0.3 M CTAB/NaCl NiO-YSZ cermet was found to be (37.8±0.8) %. Similar shrinkage values of both the electrolyte and electrodes are required to decrease the stress between the cell's components during sintering [49], thus the 0.3 M CTAB/NaCl YSZ and NiO-YSZ meet that compatibility requirement.

The dilatometry results for the 0.3 M YSZ and 0.3 M NiO-YSZ are presented in Fig. 5 (right). The thermal expansion coefficient (TEC) was determined by linear fitting (R^2=0.999) within the range marked by the dashed lines on the graph. The analysed range was narrowed down due to the slight difference in the slope of the NiO-YSZ curve, which is visible at approximately 230 °C. Such an anomaly in dilatometry measurements originates from the magnetic transition between the antiferromagnetic to paramagnetic behaviour of NiO [50,51]. Mori M. *et al.* [50] observed that even in the case of composites with only 10 vol.% NiO, the magnetic transition has a noticeable influence on the thermal expansion coefficient. The TEC values are equal $(10.84+0.03)\times10^{-6}$ K^{-1} and $(12.61+0.02)\times10^{-6}$ K^{-1} for 0.3 M CTAB/NaCl YSZ and NiO-YSZ, respectively, being in accordance with the values reported for conventional materials measured in synthetic air: $TEC_{YSZ}=(10.3\text{-}10.7)\times10^{-6}$ K^{-1}[52], $TEC_{NiO\text{-}YSZ}=(11.81\text{-}12.48)\times10^{-6}$ K^{-1} [44].

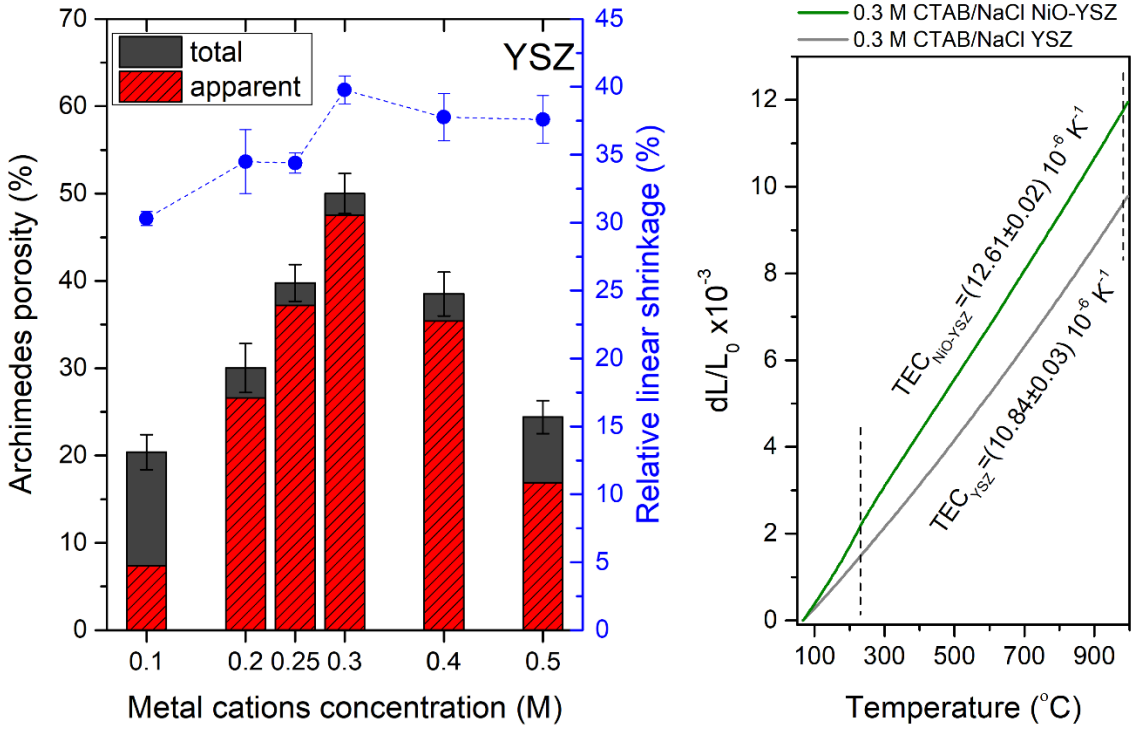

Fig. 5. Changes in 0.3 M CTAB/NaCl YSZ porosity and relative linear shrinkage based on the concentration of the starting cation in the precursor solution (left) and dilatometry results for 0.3 M CTAB/NaCl YSZ and NiO-YSZ (right). Obtained TEC values are comparable to conventional materials.

The measurement of the specific surface area (SSA) was done using the N_2 sorption technique involving the Brunauer–Emmett–Teller isotherm theory. The obtained isotherms are presented in Fig. 6 (A,C). Based on the classification of the IUPAC, all the BET isotherms were assigned to the type III isotherm with no hysteresis loop [53]. The look of the isotherms and lack of the hysteresis loop indicates that the cermets and YSZ have no microporosity and a negligible amount of mesopores. The SSA comes mostly from the overwhelming macroporosity sharply filling up when p/p_0 reaches the value of ~1. This type of isotherm is a typical example of a material where adsorbate-absorbate interactions are dominant. In this case, the energies involved in the process will come mostly from the liquefaction [54]. The formed structures are fully permeable, and no strong adsorbate-substrate interaction exists. Similar trends were observed as in case of YSZ for the cermet materials disregarding the lower SSA values caused by a higher tendency of NiO-YSZ to densify. Although the apparent porosities (see Table 1) of reduced 0.3 M CTAB/NaCl NiO-YSZ and reference sample were significantly different, the active surface area and the type of porosity were similar. However, a real development of the TPB cannot be clearly determined based on those measurements. The smaller grains of the NiO and YSZ should result in an increase of the TPB and enhance the electrochemical performance of the cells based on the 0.3 M CTAB/NaCl NiO-YSZ. The fabrication route using CTAB and NaCl can ensure high porosity with effective pore channels even if high-temperature sintering is required to provide enough mechanical strength.

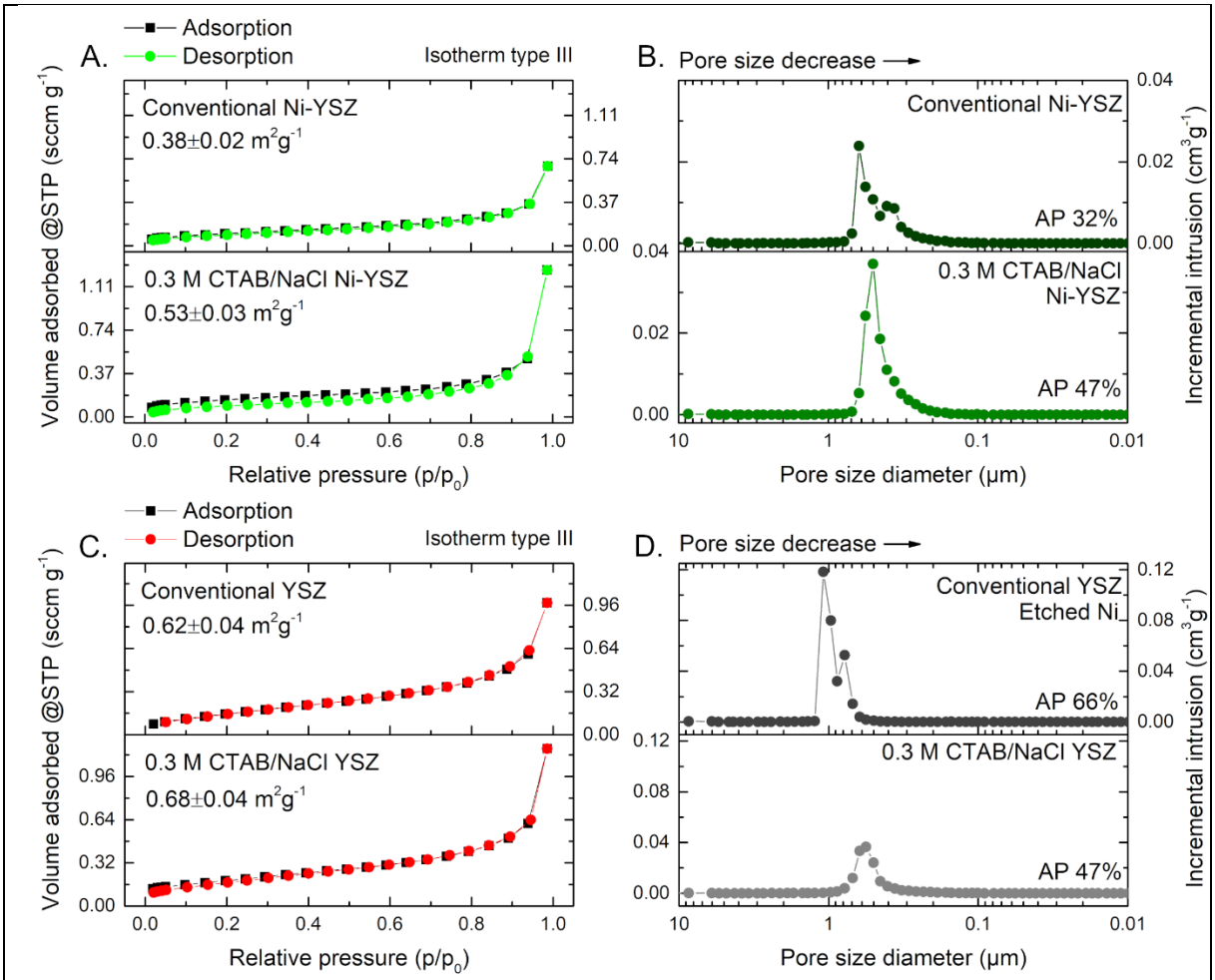

Fig. 6. BET isotherms (A,C) and pore size distribution (B,D) of the wormhole-like 0.3 M CTAB/NaCl YSZ or Ni-YSZ. Reference materials: NiO-YSZ after reduction in H_2; YSZ after reduction and etching. AP - apparent porosity; SSA calculated within 0.1-0.3 p/p_0 range.

Pore size distribution curves of the novel 0.3 M CTAB/NaCl YSZ and Ni-YSZ and conventional reference materials are plotted in Fig. 6 (B,D). The presence of two clearly distinguishable peaks, as seen for the conventional materials, originates from the two different porosity levels introduced during manufacturing of the half cells at NTUT. Compared with the reference samples, the novel composite and yttria-stabilised zirconia are characterised by a narrower and uniform pore size distribution in the 0.3–0.7 μm range with an average pore size diameter of 0.59 μm (0.3 M CTAB/NaCl YSZ) and 0.5 μm (0.3 M CTAB/NaCl Ni-YSZ). In the case of the reference YSZ obtained by etching metallic nickel from the Ni-YSZ scaffold, the pores were almost two times bigger (average diameter: 1.08 μm), while the reduced reference cermet is characterised by a similar pore size (average diameter: 0.53 μm), compared to the novel material. As can be seen, the amount of the mercury intruded differs significantly between samples, which is even more pronounced for the cumulative intrusion (see Fig. S5). The highest pore volume can be observed for the Ni-etched conventional YSZ, originating from the highest apparent porosity of the analysed samples. In case of the reduced cermet materials, the pore volume was bigger for the novel 0.3 M CTAB/NaCl Ni-YSZ, further explaining the increased total pore area. As one can see from the Tab. 1, summarising the MICP results, the CTAB/NaCl templating method leads to the formation of highly porous compounds with uniformly distributed pores. When 0.3 M of metal ions are used in the starting precursor solutions for YSZ and NiO-YSZ, the resulting total pore area and apparent porosity are approximately the same for both materials. The open porosity derived from the Hg

porosimetry is in line with the Archimedes porosity, however the porosity values are not exactly the same, which results from the use of different techniques. Although the N_2 adsorption technique is the most frequently used method to determine the specific surface area, as described in detail above, mercury intrusion porosimetry also provides information about the total pore area. When compared, the results from gas sorption and MICP differ significantly (mercury porosimetry yields considerably higher values). Such an observation should not come as a surprise, as different pore radii are accessible for these two methods and they use distinct theoretical models to calculate the specific surface area [55,56]. Therefore, it is recommended to compare those two results only in the overlapping range available for both methods. For the analysis of macroporous materials, mercury porosimetry is considered more reliable than the N_2 adsorption technique [56–58].

The electrical conductivity of the YSZ and NiO-YSZ prepared using the CTAB/NaCl-assisted route was measured via the VdP method under synthetic air and humidified H_2 (3vol.% H_2O), respectively. The results are presented in Fig. S6. The conductivity of the 0.3 M CTAB/NaCl YSZ was purely ionic and increased with the increasing temperature, reaching 0.011 S cm^{-1} at 800 °C. In contrast, the 0.3 M CTAB/NaCl NiO-YSZ composite exhibited a major contribution to the electronic conductivity in the range of around 1000 S cm^{-1}. It is a typical metallic conductivity over Ni grains in the composite structure. Disregarding the porosity, the values measured for the novel structures are within the normal conductivity ranges described widely in the literature [44,59,60].

Tab. 1. Comparison of the porosity parameters of the reference and novel YSZ and cermet materials obtained by the MICP technique. The measurement uncertainty is 5% as given by the manufacturer.

	0.3 M CTAB/NaCl YSZ	Conventional YSZ (etched Ni)	0.3 M CTAB/NaCl Ni-YSZ (after reduction in H_2)	Conventional Ni-YSZ (after reduction in H_2)
Total pore area (m^2g^{-1})	1.05	1.26	1.05	0.77
Median pore diameter by volume (μm)	0.61	1.06	0.52	0.58
Median pore diameter by area (μm)	0.57	1.01	0.49	0.46
Average pore diameter (μm)	0.59	1.09	0.51	0.53
Apparent porosity (%)	47	66	47	32

2.3. Stability and long-term performance of the novel anode

To test the deterioration rates of the novel 0.3 M CTAB/NaCl NiO-YSZ and the conventional reference cermet, a series of long-term electrical measurements were performed. The results are presented in Fig. 7 as both the measured absolute total electrical conductivity and percentage conductivity loss. Both samples were heated under flowing N_2 and flash reduced in H_2 at 800 °C for 1 h. The constant measurement of the electrical conductivity helped to visualise the deterioration of the composites under the normal working conditions of SOFCs. Despite their similar thickness (~400 μm), the samples possessed different shape of pores and porosity values, what resulted in the higher conductivity of the conventional reference material. No corrections were introduced (e.g. Bruggeman correlation) as the data was used for the comparison of the degradation rates, disregarding the absolute values of the conductivity when in bulk. A rapid drop of the conductivity is clearly noticeable within the first 24 h of the operation of the conventional anode. This is relatively normal behaviour for the standard cermet

anodes and is directly correlated to the strong coalescence and rounding up of the Ni grains and segregation of the impurities (e.g. Si) within the start-up hours of the cell [61,62]. Interestingly, no such decrease was observed with the 0.3 M CTAB/NaCl NiO-YSZ material, suggesting better initial stability and suppression of Ni structural changes throughout the anode scaffold. This is most probably due to the different shapes of the starting Ni grains, which were much more homogeneous, smaller and more rounded in shape. It was previously established by Pihlatie M. H. *et al*. [63] that the loss of percolation paths in Ni-YSZ cermet and overall degradation was mostly caused by the migration of Ni from the areas with a smaller radius of curvature to the sites with a larger radius of curvature. It was the main contribution to the initial loss in performance over ~70 h after the measurement was started. With the 0.3 M CTAB/NaCl Ni-YSZ, the more rounded, smaller, and loosely sintered NiO grains in the pre-cermet seem to partially suppress that effect. Considering only the porosity of the analysed samples, two issues can be addressed. First, the higher porosity of the 0.3 M CTAB/NaCl Ni-YSZ decreased the contact area of the adjacent Ni grains and limited the mass transfer via diffusion over the grains' surface. Second, the higher share of the voids should increase the degradation rate via the reaction of the more easily available metallic Ni particles with water vapour forming $Ni(OH)_x$. The volatile Ni hydroxide species, especially under constant polarisation, cause the coalescence of Ni via the gas phase mass transfer [62,64]. In fact, we believe that this process was not an issue for the 0.3 M CTAB/NaCl Ni-YSZ and the reference material as the water vapour concentration was rather limited.

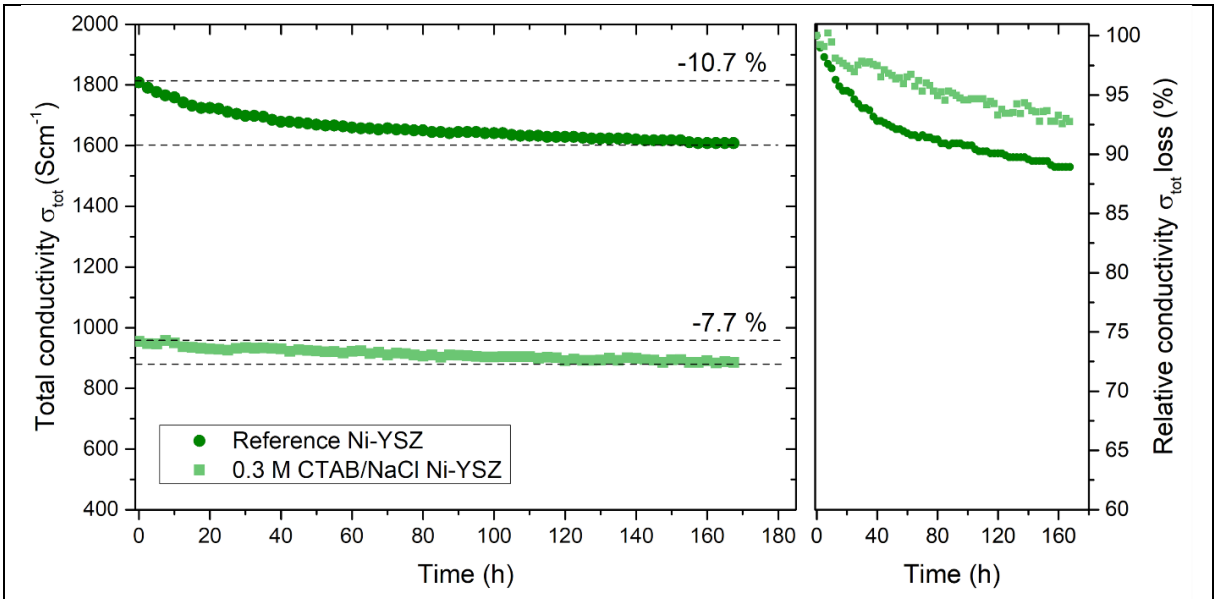

Fig. 7. Long-term electrical conductivity measurements via the VdP method under a humidified (3 vol.% H_2O) H_2 atmosphere (left) and a relative conductivity drop (right) of the 0.3 M CTAB/NaCl NiO-YSZ and the reference anode.

The YSZ backbone structure has a crucial influence on the Ni migration as the coalescence and the destruction of conduction paths takes place right after the loss of contact between the YSZ and Ni [62,65]. A higher level of integration at the interface and better wettability of the Ni at the YSZ surface stabilise the 0.3 M CTAB/NaCl Ni-YSZ and thus suppress massive growth of Ni grains during the operation. It can all be tailored during the preparation steps and highlights the essential role of the microstructure in the cells' performance.

To better understand the mechanism of the degradation, a series of structural analyses was performed using SEM imaging at the polished cross-sections of both anodes coupled with the EDS spatial elemental maps. The results are presented in Fig. 8. It is clearly noticeable that the 0.3 M CTAB/NaCl Ni-YSZ (reduced) had smaller initial grains of both Ni and YSZ compared to the reference sample. It was much

easier to observe this with the Ni grains, which exhibited an interesting three-dimensional structure finely dispersed within the YSZ backbone. This microstructure can ensure the strong development of the TPB so badly needed for the electrochemical reactions to happen [66]. Even though the composite grains are smaller than with the ball-milled conventional structure, it is clearly evidenced that there are well established ionic and electronic paths, and no isolated YSZ or Ni islands are clearly observable. The main advantages of the CTAB/NaCl-assisted synthesis route are smaller particles of Ni/YSZ, high homogeneity, highly developed TPB (based on the SEM images), and better interfacial interaction between the ionic and electronic conductors. Post-mortem characterisation was performed for the same samples after the 160 h ageing tests. While no depletion of the Ni was encountered (based on the EDS), the visual comparison of the elemental maps before and after 160 h of ageing under the humidified H_2 atmosphere revealed a significant Ni coarsening, which happened especially in the case of the reference sample. For the 0.3 M CTAB/NaCl Ni-YSZ, the effect of Ni agglomeration was minor, and the structure remained similar to the pristine one.

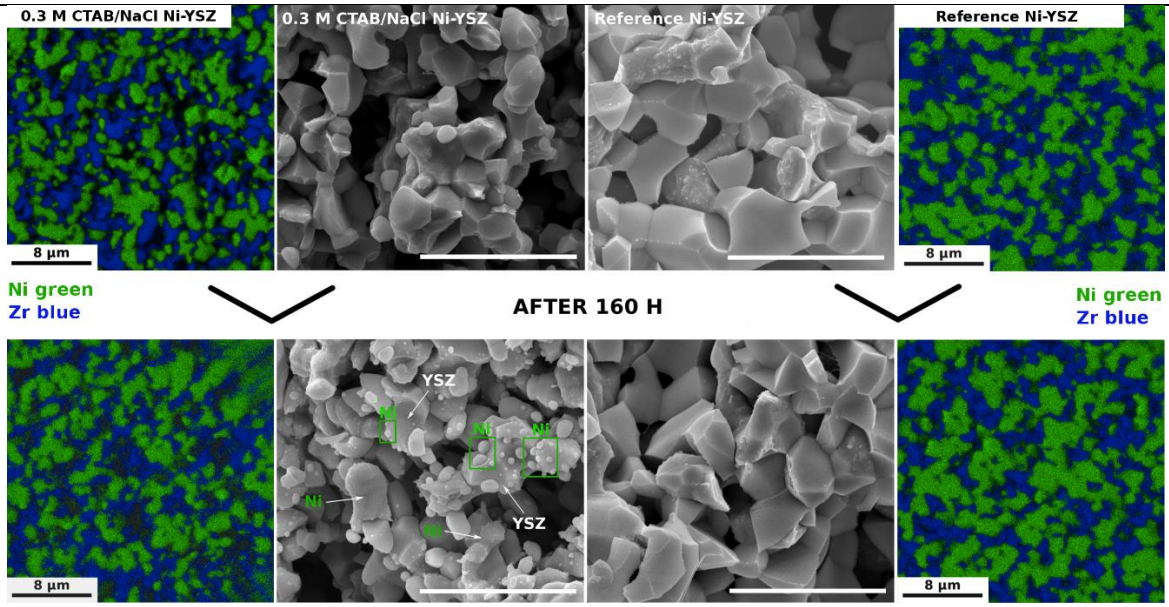

Fig. 8. SEM images and EDS elemental maps of the 0.3 M CTAB/NaCl Ni-YSZ (reduced) and conventional reference anodes before and after the ageing tests. Scale bar is 8 µm each time. Clear evidence of the Ni grains growth in the reference material was observed.

The homogeneous distribution of both phases was maintained for both samples, but with the 0.3 M CTAB/NaCl Ni-YSZ, the sizes of the grains and the porosity channels do not change drastically. The degradation of the reference sample was clearly caused by the strong agglomeration and sintering of the Ni grains, which resulted in the partial loss of the conduction paths. At the same time, the reference sample decreased the amount of observed pore channels. It is also worth mentioning that the 0.3 M CTAB/NaCl NiO-YSZ underwent complete phase decomposition after the prolonged reduction time. This was evidenced by the Ni submicrometric spherical agglomerates that formed on the surface of YSZ grains (see Fig. 8, centre bottom). In the long run, this could be beneficial for the operation of the real-life cell, as the formed particles of metallic Ni may function as active sites for oxidation reactions. To further prove this, a series of symmetrical and full-cell measurements will be performed in future studies. The bulk Ni grains of the novel cermet material remained of a similar, rounded shape after the ageing test and no clear view of the loss in the Ni-YSZ connection was visible on the spent sample.

Based on the post-mortem microstructural analysis, it can be stated that the novel CTAB/NaCl-assisted method of obtaining NiO-YSZ composites is a very promising route to enhance the stability and, possibly, the activity of SOFC anodes. At the same time, the addition of sacrificial pore formers was not

needed to obtain a highly porous structure, which increases the eco-friendly character of the fabrication route. Using the presented method, it is possible to form very thin pellets of less than 400 μm via simple single-axis powder pressing. Further research will focus on the measurements of the real-life electrochemical activity of the novel material when in contact with the rest of the cell's components. Furthermore, the studies will also include the changes in the YSZ:NiO volume ratio in the composite to further limit the degradation rate via the stabilising effect of the wormhole-like structure. It is predicted that decreased NiO amount coupled with the very high dispersion and homogeneity of the NiO grains will ensure high electronic conductivity and an even more pronounced limitation of the deterioration rate.

4. Conclusions

In this study, a series of YSZ and NiO-YSZ composites were fabricated via a novel synthesis route involving the co-precipitation of metal hydroxides in the presence of micelle-forming agents. After the precipitation, the gel was supported on a soft micelle-based template to be further structured via leftover NaCl formed during the drying step (hard template). The co-existence of those two templates resulted in obtaining a wormhole-like structure of either YSZ or NiO-YSZ, depending on the starting cation composition. It was evidenced that the concentration of 0.3 M cations in the starting solution gave the most homogeneous structure with the highest porosity of around 50% and 47% for 8YSZ and NiO-YSZ (reduced), respectively, even though no additional pore formers were added. The NiO-YSZ is composed of two distinctive phases, but the partial dissolution of NiO into YSZ lattice was observed. The reduction of the NiO-YSZ composite led to the full separation of both phases. The reduction studies proved that the novel way to prepare NiO-YSZ ensures a higher degree of integration of the NiO and YSZ grains and limits the growth of Ni grains during redox cycles. The materials were characterised by matching TEC values and a well-established pore channel structure, which was fully permeable for the reactant gases. The long-run electrical conductivity test revealed that 0.3 M CTAB/NaCl NiO-YSZ is more stable within 160 h of testing than the corresponding reference material prepared using conventional methods (7.7 vs 10.7% total conductivity loss). It was found that the restructured material is less prone to Ni agglomeration and migration across the anode, mostly due to the increased NiO-YSZ interfacial integration as well as uniform and finely dispersed Ni grains after reduction. The novel soft-hard templating method may be a promising route for fabricating functional ceramics with improved stability thanks to the tailored microstructure alteration.

Acknowledgements

This work was supported by a project funded by National Science Centre Poland, based on decision 2017/25/B/ST8/02275. We acknowledge SOLARIS Centre for access to the Beamline DEMETER, where the measurements were performed. The MICP research was partly funded by a statutory research program at the Faculty of Geology, Geophysics and Environmental Protection, AGH University of Science and Technology in Krakow, Poland, statutory work No. 16.16.140.315/05.

Literature

[1] T. Talebi, M.H. Sarrafi, M. Haji, B. Raissi, A. Maghsoudipour, Investigation on microstructures of NiO–YSZ composite and Ni–YSZ cermet for SOFCs, Int. J. Hydrogen Energy. 35 (2010) 9440–9447. https://doi.org/https://doi.org/10.1016/j.ijhydene.2010.04.156.

[2] E.W. Park, H. Moon, M. soo Park, S.H. Hyun, Fabrication and characterization of Cu-Ni-YSZ SOFC anodes for direct use of methane via Cu-electroplating, Int. J. Hydrogen Energy. 34 (2009) 5537–5545. https://doi.org/10.1016/j.ijhydene.2009.04.060.

[3] S. Hussain, L. Yangping, Review of solid oxide fuel cell materials: cathode, anode, and electrolyte, Energy Transitions. (2020). https://doi.org/10.1007/s41825-020-00029-8.

[4] H.J. Cho, G.M. Choi, Effect of milling methods on performance of Ni-Y2O3-stabilized ZrO2 anode for solid oxide fuel cell, J. Power Sources. 176 (2008) 96–101. https://doi.org/10.1016/j.jpowsour.2007.09.118.

[5] J.-H. Lee, H. Moon, H.-W. Lee, J. Kim, J.-D. Kim, K.-H. Yoon, Quantitative analysis of microstructure and its related electrical property of SOFC anode, Ni–YSZ cermet, Solid State Ionics. 148 (2002) 15–26. https://doi.org/https://doi.org/10.1016/S0167-2738(02)00050-4.

[6] V. Esposito, D.Z. de Florio, F.C. Fonseca, E.N.S. Muccillo, R. Muccillo, E. Traversa, Electrical properties of YSZ/NiO composites prepared by a liquid mixture technique, J. Eur. Ceram. Soc. 25 (2005) 2637–2641. https://doi.org/10.1016/j.jeurceramsoc.2005.03.116.

[7] D. Simwonis, F. Tietz, D. Stöver, Nickel coarsening in annealed Ni/8YSZ anode substrates for solid oxide fuel cells, Solid State Ionics. 132 (2000) 241–251. https://doi.org/10.1016/s0167-2738(00)00650-0.

[8] M. Liang, B. Yu, M. Wen, J. Chen, J. Xu, Y. Zhai, Preparation of NiO–YSZ composite powder by a combustion method and its application for cathode of SOEC, Int. J. Hydrogen Energy. 35 (2010) 2852–2857. https://doi.org/https://doi.org/10.1016/j.ijhydene.2009.05.006.

[9] M. Kishimoto, K. Miyawaki, H. Iwai, M. Saito, H. Yoshida, Effect of composition ratio of Ni-YSZ anode on distribution of effective three-phase boundary and power generation performance, Fuel Cells. 13 (2013) 476–486. https://doi.org/10.1002/fuce.201200174.

[10] S. Lee, K.H. Kang, H.S. Hong, Y.S. Yun, S.K. Woo, Performance of Ni/YSZ cermet cathode prepared by mechanical alloying for high temperature electrolysis of water vapor (steam): Effect of anode and cathode thicknesses on the efficiency of hydrogen production, Zeitschrift Fuer Met. Res. Adv. Tech. 99 (2008) 114–119. https://doi.org/10.3139/146.101613.

[11] A. Pesce, A. Hornés, M. Núñez, A. Morata, M. Torrell, A. Tarancón, 3D printing the next generation of enhanced solid oxide fuel and electrolysis cells, J. Mater. Chem. A. 8 (2020) 16926–16932. https://doi.org/10.1039/d0ta02803g.

[12] B. Kim, K. Cho, J. Choi, D. Shin, Preparation of NiO-YSZ Composite Powder Through 2-Step Hydrothermal Synthesis and Its Application to Solid Oxide Fuel Cell Anode Functional Layer, J. Nanosci. Nanotechnol. 15 (2015). https://doi.org/10.1166/jnn.2015.8400.

[13] J.H. Song, M.Y. Park, H.W. Park, H.T. Lim, Single-step preparation of nano-homogeneous NiO/YSZ composite anode for solid oxide fuel cells, Nano-Micro Lett. 5 (2013) 111–116. https://doi.org/10.5101/nml.v5i2.p111-116.

[14] K. Miyamoto, H. Koga, M. Izumi, M. Mizui, H. Nishiguchi, Study on Fabrication of Anodes for SOFCs with 3D Printing Technology, ECS Trans. 96 (2020) 219–226. https://doi.org/10.1149/09601.0219ecst.

[15] J.C. Ruiz-Morales, A. Tarancón, J. Canales-Vázquez, J. Méndez-Ramos, L. Hernández-Afonso, P. Acosta-Mora, J.R. Marín Rueda, R. Fernández-González, Three dimensional printing of components and functional devices for energy and environmental applications, Energy Environ. Sci. 10 (2017) 846–859. https://doi.org/10.1039/c6ee03526d.
[16] I. Jang, G.H. Kelsall, Fabrication of 3D NiO-YSZ structures for enhanced performance of solid oxide fuel cells and electrolysers, Electrochem. Commun. 137 (2022) 107260. https://doi.org/10.1016/j.elecom.2022.107260.
[17] U. Betke, K. Schelm, A. Rodak, M. Scheffler, Cellular Nickel-Yttria/Zirconia (Ni–YSZ) Cermet Foams: Manufacturing, Microstructure and Properties, Materials (Basel). 13 (2020). https://doi.org/10.3390/ma13112437.
[18] S. Li, R. Guo, J. Li, Y. Chen, W. Liu, Synthesis of NiO–ZrO2 powders for solid oxide fuel cells, Ceram. Int. 29 (2003) 883–886. https://doi.org/https://doi.org/10.1016/S0272-8842(03)00031-2.
[19] R.F. Martins, M.C. Brant, R.Z. Domingues, R.M. Paniago, K. Sapag, T. Matencio, Synthesis and characterization of NiO-YSZ for SOFCs, Mater. Res. Bull. 44 (2009) 451–456. https://doi.org/10.1016/j.materresbull.2008.04.017.
[20] J.F.L. Imperial, R.B. Cervera, Synthesis and Characterization of Porous NiO/YSZ Electrode Materials Using Different Pore Formers, Mater. Sci. Forum. 917 (2018) 83–87. https://doi.org/10.4028/www.scientific.net/MSF.917.83.
[21] T. de Terris, O. Andreau, P. Peyre, F. Adamski, I. Koutiri, C. Gorny, C. Dupuy, Optimization and comparison of porosity rate measurement methods of Selective Laser Melted metallic parts, Addit. Manuf. 28 (2019) 802–813. https://doi.org/10.1016/j.addma.2019.05.035.
[22] M. Frauscher, C. Besser, G. Allmaier, N. Dörr, Elucidation of oxidation and degradation products of oxygen containing fuel components by combined use of a stable isotopic tracer and mass spectrometry, Anal. Chim. Acta. 993 (2017) 47–54. https://doi.org/10.1016/j.aca.2017.09.009.
[23] S.P. Moulik, B. Naskar, A.K. Rakshit, Current status of enthalpy-entropy compensation phenomenon, Curr. Sci. 117 (2019) 1286–1291. https://doi.org/10.18520/cs/v117/i8/1286-1291.
[24] X. Sun, S.K. Dey, Insights into the Synthesis of Layered Double Hydroxide (LDH) Nanoparticles: Part 2. Formation Mechanisms of LDH, J Colloid Interface Sci. 458 (2015) 160–168. https://doi.org/10.1016/j.jcis.2015.06.025.
[25] T. Götsch, W. Wallisch, M. Stöger-Pollach, B. Klötzer, S. Penner, From zirconia to yttria: Sampling the YSZ phase diagram using sputter-deposited thin films, AIP Adv. 6 (2016). https://doi.org/10.1063/1.4942818.
[26] B. Budiana, F. Fitriana, N. Ayu, S. Suasmoro, Preparation and conductivity measurement of 7-8 mol % YSZ and 12 mol % CSZ for electrolyte SOFC, J. Phys. Conf. Ser. 739 (2016) 6–12. https://doi.org/10.1088/1742-6596/739/1/012022.
[27] S. Linderoth, N. Bonanos, Effects of Dissolution and Exsolution of Ni in YSZ, Mater. Electrochem. Energy Convers. Storage. (2002). https://doi.org/10.1002/9781118370858.ch16.
[28] S. Joo, C. Lim, O. Kwon, L. Zhang, J. Zhou, J.-Q. Wang, H.Y. Jeong, Y. Sin, S. Choi, G. Kim, The first observation of Ni nanoparticle exsolution from YSZ and its application for dry reforming of methane, Mater. Reports Energy. 1 (2021) 100021. https://doi.org/10.1016/j.matre.2021.100021.
[29] Y.M. Park, G.M. Choi, Mixed Ionic and Electronic Conduction in YSZ-NiO Composite, J. Electrochem. Soc. 146 (1999) 883–889. https://doi.org/10.1149/1.1391696.
[30] A. Kuzjukevics, S. Linderoth, Interaction of NiO with yttria-stabilized zirconia, Solid

State Ionics. 93 (1997) 255–261. https://doi.org/10.1016/s0167-2738(96)00529-2.
[31] A.K. Soman, P. Kuppusami, A.M. Rabel, Electrical Conductivity of NiO-Gadolinia Doped Ceria Anode Material for Intermediate Temperature Solid Oxide Fuel Cells, Nano Hybrids Compos. 17 (2017) 224–236. https://doi.org/10.4028/www.scientific.net/nhc.17.224.
[32] J. Bandyopadhyay, K.P. Gupta, Low temperature lattice parameter of nickel and some nickel-cobalt alloys and Grüneisen parameter of nickel, Cryogenics (Guildf). 17 (1977) 345–347. https://doi.org/10.1016/0011-2275(77)90130-8.
[33] I.Y. Kaplin, E.S. Lokteva, E. V Golubina, K.I. Maslakov, N.E. Strokova, S.A. Chernyak, V. V Lunin, Sawdust as an effective biotemplate for the synthesis of Ce0.8Zr0.2O2 and CuO-Ce0.8Zr0.2O2 catalysts for total CO oxidation, RSC Adv. 7 (2017) 51359–51372. https://doi.org/10.1039/c7ra10791a.
[34] X. Wang, H. Xie, R. Du, Y. Liu, P. Lin, J. Zhang, C. Bu, Y. Huang, W. Zhang, High-temperature chlorination of PbO and CdO induced by interaction with NaCl and Si/Al matrix, (2018). https://doi.org/10.1039/c8ra06255b.
[35] C.A.A. Rocha, G.C. Cordeiro, R.D.T. Filho, Use of thermal analysis to determine the hydration products of oil well cement pastes containing NaCl and KCl, J. Therm. Anal. Calorim. 122 (n.d.) 1279–1288. https://doi.org/10.1007/s10973-015-4949-6.
[36] D.R. Lide, CRC Handbook of Chemistry and Physics, 84th edition, CRC Press. 84 (2003). https://doi.org/10.1136/oem.53.7.504.
[37] R.M. Batista, E.N.S. Muccillo, Densification and grain growth of 8YSZ containing NiO, Ceram. Int. 37 (2011) 1047–1053. https://doi.org/10.1016/j.ceramint.2010.11.031.
[38] Y. Zhang, B. Liu, B. Tu, Y. Dong, M. Cheng, Redox cycling of Ni – YSZ anode investigated by TPR technique, 176 (2005) 2193–2199. https://doi.org/10.1016/j.ssi.2005.06.016.
[39] H. Mori, C.J. Wen, J. Otomo, K. Eguchi, H. Takahashi, Investigation of the interaction between NiO and yttria-stabilized zirconia (YSZ) in the NiO/YSZ composite by temperature-programmed reduction technique, Appl. Catal. A Gen. 245 (2003) 79–85. https://doi.org/10.1016/S0926-860X(02)00634-8.
[40] A.A. Lopera, E.A. Chavarriaga, J.A. Perez-Taborda, S.L. Amaya, A. Echavarría, C. García, Effect of the Fuel in the Synthesis of NiO–YSZ by Solution Combustion Synthesis with Potential Application in Catalysis of Hydrogen, Int. J. Self-Propagating High-Temperature Synth. 31 (2022) 74–79. https://doi.org/10.3103/s1061386222020042.
[41] X. Hu, J. Yang, W. Sun, N. Wang, S. An, Q. Wang, Y. Zhang, X. Xie, L. Huang, Y-Zr-O solid solution supported Ni-based catalysts for hydrogen production via auto-thermal reforming of acetic acid, Appl. Catal. B Environ. 278 (2020) 119264. https://doi.org/10.1016/j.apcatb.2020.119264.
[42] J.T. White, I.E. Reimanis, J.R. O'Brien, Solubility of NiO in pechini-derived ZrO 2 examined with SQUID magnetometry, J. Mater. Sci. 47 (2012) 1690–1696. https://doi.org/10.1007/s10853-011-5839-3.
[43] H. Mori, C. Wen, J. Otomo, K. Eguchi, H. Takahashi, Investigation of the interaction between NiO and yttria-stabilized zirconia (YSZ) in the NiO/YSZ composite by temperature-programmed reduction technique, 245 (2003) 79–85. https://doi.org/10.1016/S0926-860X(02)00634-8.
[44] D.A. Osinkin, D.I. Bronin, S.M. Beresnev, N.M. Bogdanovich, V.D. Zhuravlev, G.K. Vdovin, T.A. Demyanenko, Thermal expansion, gas permeability, and conductivity of Ni-YSZ anodes produced by different techniques, J. Solid State Electrochem. 18 (2014) 149–156. https://doi.org/10.1007/s10008-013-2239-4.
[45] D. Jing, H. Li, X.U. Liping, Z. Lei, W. Guangwei, Preparation of YSZ solid electrolyte

by slip casting and its properties, RARE Met. 28 (2009) 372. https://doi.org/10.1007/s12598-009-0074-7.
[46] L. Hu, C.-A. Wang, Effect of sintering temperature on compressive strength of porous yttria-stabilized zirconia ceramics, Ceram. Int. 36 (2010) 1697–1701. https://doi.org/10.1016/j.ceramint.2010.03.009.
[47] V.D. Zhuravlev, Y.I. Komolikov, L. V Ermakova, Correlations among sintering temperature, shrinkage, and open porosity of 3.5 YSZ/Al 2 O 3 composites, Ceram. Int. 42 (2016) 8005–8009. https://doi.org/10.1016/j.ceramint.2016.01.204.
[48] D. Panthi, N. Hedayat, Y. Du, Densification behavior of yttria-stabilized zirconia powders for solid oxide fuel cell electrolytes, J. Adv. Ceram. 7 (2018) 325–335. https://doi.org/10.1007/s40145-018-0282-4.
[49] A.M. Balagurov, I.A. Bobrikov, S. V Sumnikov, V.Y. Yushankhai, N. Mironova-Ulmane, Magnetostructural Phase Transitions in NiO and MnO: Neutron Diffraction Data, JETP Lett. 104 (2016) 84–90. https://doi.org/10.1134/S0021364016140071.
[50] M. Mori, T. Yamamoto, H. Itoh, H. Inaba, H. Tagawa, Thermal Expansion of Nickel-Zirconia Anodes in Solid Oxide Fuel Cells during Fabrication and Operation, J. Electrochem. Soc. 145 (1998) 1374.
[51] H. Inaba, Semi-Empirical Estimation of Thermal Expansion Coefficients of Oxides, Jpn. J. Appl. Phys. 35 (1996) 4735.
[52] X.Q. Cao, R. Vassen, D. Stoever, Ceramic materials for thermal barrier coatings, J. Eur. Ceram. Soc. 24 (2004) 1–10. https://doi.org/10.1016/S0955-2219(03)00129-8.
[53] S. Brunauer, L.S. Deming, W.E. Deming, E. Teller, On a Theory of the van der Waals Adsorption of Gases, J. Am. Chem. Soc. 62 (1940) 1723–1732. https://doi.org/10.1021/ja01864a025.
[54] K.V. Kumar, S. Gadipelli, B. Wood, K.A. Ramisetty, A.A. Stewart, C.A. Howard, D.J.L. Brett, F. Rodriguez-Reinoso, Characterization of the adsorption site energies and heterogeneous surfaces of porous materials, J. Mater. Chem. A. 7 (2019) 10104–10137. https://doi.org/10.1039/c9ta00287a.
[55] A. Bogner, J. Schatz, F. Dehn, H.S. Müller, Influence of Drying on the Microstructure of Hardened Cement Paste: A Mercury Intrusion Porosimetry, Nitrogen Sorption and SAXS Study, J. Adv. Concr. Technol. 18 (2020) 83–94. https://doi.org/10.3151/jact.18.83.
[56] M. Hasanuzzaman, A.R.M. Harunur Rashid, A.-G. Olabi, Characterization of Porous Glass and Ceramics by Mercury Intrusion Porosimetry, Ref. Modul. Mater. Sci. Mater. Eng. (2017). https://doi.org/10.1016/B978-0-12-803581-8.09266-3.
[57] J. Rouquerol, G. V. Baron, R. Denoyel, H. Giesche, J. Groen, P. Klobes, P. Levitz, A. V. Neimark, S. Rigby, R. Skudas, K. Sing, M. Thommes, K. Unger, The characterization of macroporous solids: An overview of the methodology, Microporous Mesoporous Mater. 154 (2012) 2–6. https://doi.org/10.1016/J.MICROMESO.2011.09.031.
[58] J. Rouquerol, G. Baron, R. Denoyel, H. Giesche, J. Groen, P. Klobes, P. Levitz, A. V. Neimark, S. Rigby, R. Skudas, K. Sing, M. Thommes, K. Unger, Liquid intrusion and alternative methods for the characterization of macroporous materials (IUPAC technical report), Pure Appl. Chem. 84 (2012) 107–136. https://doi.org/10.1351/PAC-REP-10-11-19/MACHINEREADABLECITATION/RIS.
[59] N. Arifin, T. Button, R. Steinberger-Wilckens, Carbon-Tolerant Ni/ScCeSZ via Aqueous Tape Casting for IT- SOFCs, ECS Trans. 78 (2017) 1417–1425. https://doi.org/10.1149/07801.1417ecst.
[60] C.T. Shen, K.R. Lee, Y.P. Hsieh, S.W. Lee, J.K. Chang, S.C. Jang, C.J. Tseng, Effects of TiO2 and SDC addition on the properties of YSZ electrolyte, Int. J. Hydrogen Energy. 44 (2019) 29426–29431. https://doi.org/10.1016/j.ijhydene.2019.07.051.

[61] P. Błaszczak, M. Łapiński, S.F. Wang, P. Jasiński, B. Bochentyn, Exsolution of Ni nanoparticles on the surface of cerium and nickel co-doped lanthanum strontium titanate as a new anodic layer for DIR-SOFC. Anti-coking potential and H2S poisoning resistance of the prepared material, Int. J. Hydrogen Energy. 45 (2020) 29186–29200. https://doi.org/10.1016/j.ijhydene.2020.07.162.
[62] M.B. Mogensen, A. Hauch, X. Sun, M. Chen, Y. Tao, S.D. Ebbesen, K. V. Hansen, P. V. Hendriksen, Relation Between Ni Particle Shape Change and Ni Migration in Ni–YSZ Electrodes – a Hypothesis, Fuel Cells. 17 (2017) 434–441. https://doi.org/10.1002/fuce.201600222.
[63] M.H. Pihlatie, A. Kaiser, M. Mogensen, M. Chen, Electrical conductivity of Ni-YSZ composites: Degradation due to Ni particle growth, Solid State Ionics. 189 (2011) 82–90. https://doi.org/10.1016/j.ssi.2011.02.001.
[64] A. Hauch, S.D. Ebbesen, S.H. Jensen, M. Mogensen, Solid Oxide Electrolysis Cells: Microstructure and Degradation of the Ni/Yttria-Stabilized Zirconia Electrode, J. Electrochem. Soc. 155 (2008) B1184. https://doi.org/10.1149/1.2967331.
[65] S.J. McPhail, S. Frangini, J. Laurencin, E. Effori, A. Abaza, A.K. Padinjarethil, A. Hagen, A. Léon, A. Brisse, D. Vladikova, B. Burdin, F.R. Bianchi, B. Bosio, P. Piccardo, R. Spotorno, H. Uchida, P. Polverino, E.A. Adinolfi, F. Postiglione, J. Lee, H. Moussaoui, J. Van herle, Addressing planar solid oxide cell degradation mechanisms: A critical review of selected components, Electrochem. Sci. Adv. (2021) 1–37. https://doi.org/10.1002/elsa.202100024.
[66] F.S. da Silva, T.M. de Souza, Novel materials for solid oxide fuel cell technologies: A literature review, Int. J. Hydrogen Energy. 42 (2017) 26020–26036. https://doi.org/10.1016/j.ijhydene.2017.08.105.